ENGINEERING

Real-time 3D optoacoustic tracking of cell-sized magnetic microrobots circulating in the mouse brain vasculature

Paul Wrede[1,2,3], Oleksiy Degtyaruk[1,2], Sandeep Kumar Kalva[1,2], Xosé Luis Deán-Ben[1,2], Ugur Bozuyuk[3], Amirreza Aghakhani[3], Birgul Akolpoglu[3], Metin Sitti[2,3,4]*, Daniel Razansky[1,2]*

Mobile microrobots hold remarkable potential to revolutionize health care by enabling unprecedented active medical interventions and theranostics, such as active cargo delivery and microsurgical manipulations in hard-to-reach body sites. High-resolution imaging and control of cell-sized microrobots in the in vivo vascular system remains an unsolved challenge toward their clinical use. To overcome this limitation, we propose noninvasive real-time detection and tracking of circulating microrobots using optoacoustic imaging. We devised cell-sized nickel-based spherical Janus magnetic microrobots whose near-infrared optoacoustic signature is enhanced via gold conjugation. The 5-, 10-, and 20-μm-diameter microrobots are detected volumetrically both in bloodless ex vivo tissues and under real-life conditions with a strongly light-absorbing blood background. We further demonstrate real-time three-dimensional tracking and magnetic manipulation of the microrobots circulating in murine cerebral vasculature, thus paving the way toward effective and safe operation of cell-sized microrobots in challenging and clinically relevant intravascular environments.

INTRODUCTION

The vision of precise and targeted medical interventions within the human body has prompted the development of mobile microrobots to perform various medical tasks (*1*, *2*). Owing to their size range of a few micrometers up to tens or hundreds of micrometers, they can be navigated across hard-to-reach regions of the body such as small vessels and bile ducts. Their potential medical applications range from targeted drug (*3*–*10*), cell (*11*–*13*), and gene delivery (*14*) to minimally invasive diagnosis (*15*), blood clot removal (*16*–*18*), and targeted hyperthermia (*19*, *20*). The circulatory system supplies all organs and tissues and thus provides an ideal route for microrobots to reach various deep target locations. The microcapillary diameter of down to 8 μm in humans requires the use of microcapillary-sized microrobots to allow safe operation in the vascular system (*21*). Considering also the relatively high blood flow velocity, in vivo detection, tracking, and actuation of microrobots remain an arduous endeavor (*22*). To overcome the harsh blood flow conditions, several studies proposed sophisticated microrobot propulsion mechanisms to move under physiological blood flows (*11*, *23*, *24*). While microrobot actuation has seen substantial progress in the recent years, three-dimensional (3D) real-time tracking of cell-sized robots, especially in the vascular system, has not been accomplished in physiologically relevant conditions. The small size of single microrobots makes their detection and tracking extremely challenging yet indispensable for achieving precise navigation, control, and validation of therapeutic interventions. Hence, a fundamental need exists for high-resolution, real-time 3D tracking of microrobots to facilitate their translation to clinics.

To this end, several studies presented tracking of micro- and millirobots using established medical imaging modalities, such as magnetic resonance imaging (*25*), x-ray computed tomography (*26*), ultrasound (US) (*27*), optical imaging (*28*, *29*), and positron emission tomography (*30*). However, sensitive detection and 3D tracking of microrobots in the vascular system is hampered by their small size and inadequate spatiotemporal resolution of the imaging systems. Optoacoustic tomography (OAT) has recently been proposed as an emerging modality for fast tracking of microrobots. It is based on the photophonic effect (*31*, *32*), where US waves induced by absorption of nanosecond-pulsed laser light in tissues are detected with broadband US transducers. In contrast to optical microscopy, OAT is based on diffuse (unfocused) light excitation, while image formation is achieved via US (acoustic) inversion. When operated in the near-infrared (NIR) wavelength range, OAT was shown capable of fully noninvasive (skull and scalp intact) imaging of the whole mouse brain with high contrast and high spatiotemporal resolution. In particular, OAT imaging at the whole murine organ scale can be accomplished with 3D spatial resolution down to 100 μm and 100-Hz volume rates (*33*), which may potentially enable real-time 3D tracking and control of microrobots in real biological environments. In addition, OAT can be used to gain molecular information about the microrobot environment (*34*–*37*), thereby efficiently monitoring the therapeutic process.

Sensitive high-resolution detection of cell-sized microrobots within the vascular system by means of OAT is challenging due to several factors. First, the whole-blood present in the vasculature generates excessive background optoacoustic signals due to the high concentration of hemoglobin, thus shadowing the signals generated by contrast agents. Second, cell-sized microrobots offer only a limited surface area. Consequently, only a small amount of chromophoric substance is available on each robot for absorbing the incoming NIR light pulses, thus weakening the generated signal intensity. Last, mammalian tissues exhibit strong optical absorption and scattering, especially in the visible light spectrum (*38*). This

[1]Institute of Pharmacology and Toxicology and Institute for Biomedical Engineering, Faculty of Medicine, University of Zurich, 8057 Zurich, Switzerland. [2]Institute for Biomedical Engineering, Department of Information Technology and Electrical Engineering, ETH Zurich, 8093 Zurich, Switzerland. [3]Physical Intelligence Department, Max Planck Institute for Intelligent Systems, 70569 Stuttgart, Germany. [4]School of Medicine and College of Engineering, Koç University, Istanbul 34450, Turkey.
*Corresponding author. Email: sitti@is.mpg.de (M.S.); daniel.razansky@uzh.ch (D.R.)

leads to strong light attenuation and diminished light intensity reaching deep tissues, further contributing to the weak signal levels available for detection by the OAT.

The potential of OAT for monitoring large microrobots has been showcased by tracking clusters of micromotors embedded into around 1-mm-diameter polyethylene capsules inside the gastrointestinal tract of mice (*39*). Another study showed the visualization of 100-μm-long helical microrobots inside phantoms and ex vivo chicken breasts (*40*). OAT was used to visualize FePt-coated spherical microrobots that were directly injected into the muscular tissue of a dead mouse (*41*). The visualized particle agglomeration consisted of around 30,000 individual microrobots while the image acquisition took 45 min due to the low optical absorption contrast exhibited by the robots that were not optimized for sensitive OAT detection. The tracking of swarms and individual helical microrobots within the bladder and uterus of mice using hybrid high-frequency US and OAT were also demonstrated (*42*). Besides microparticle-based and helical microrobots, a swarm of bacteria-based microrobots was tracked in vivo following their subcutaneous injection (*43*). Those were visible in a cluster consisting of approximately 30,000 microrobots, each sized around 100 μm. These large dimensions limit applicability of these microrobots to relatively large bodily cavities. However, for safe circulation inside the human vascular system, the microrobot diameter must be kept around 5 to 10 μm, similar to the size of red blood cells. Even in the case of soft-bodied deformable microrobots, their size should not exceed 10 to 20 μm to allow for safe travel through capillaries (*22*). Moreover, the insufficient optical absorption contrast of microrobot materials used in previous studies has restricted the monitoring ability to large-sized robots or otherwise large particle agglomerates under ex vivo conditions (*41*). Last, no simultaneous actuation and tracking under OAT have so far been demonstrated.

Here, we devise a range of microcapillary-sized microrobots featuring indocyanine green (ICG)–entrapped nanoliposome [liposome ICG (Lipo-ICG)] and golden (Au) coatings, the latter mainly contributing to enhancement of their optoacoustic signature in the NIR light spectrum for deep tissue imaging (Fig. 1, A and B). Real-time volumetric OAT imaging of circulating microrobots with diameters ranging from 5 to 20 μm is demonstrated in ex vivo porcine heart vessel phantoms and inside murine cerebral vasculature under realistic conditions of highly absorbing blood background. The small size of the microrobots further enables their effective propulsion and magnetic manipulation inside vasculature (Fig. 1C). The proposed approach thus paves the way toward more sophisticated microrobotic applications in challenging and clinically relevant intravascular environments.

RESULTS

Microrobot synthesis and characterization

The devised microrobots are based on a silica particle core coated with a 120-nm-thick layer of Ni and 50-nm-thick Au by sequential sputtering, resulting in a Janus-type particle. A second group of microrobots was additionally coated with Lipo-ICG conjugated to the remaining bare silica part. Both Au and ICG molecules are known to enhance the OAT imaging contrast (*33*). Below these two groups are referred as non-ICG–coated and ICG-coated microrobots. For further details on the fabrication process, we refer to Materials and Methods.

In OAT, the detected signal is proportional to the wavelength-dependent optical absorption properties. Blood and mammalian tissues in general exhibit relatively low absorption in the NIR (700 to 1100 nm) spectral region, thus facilitating deep tissue imaging of contrast-enhancing moieties. To analyze the absorbance spectra of the coated microrobots, optical spectroscopy measurements were performed (Fig. 2A). In the 600- to 670-nm wavelength range, both types of microrobots manifest similar spectral behavior except that the ICG-coated microrobots exhibit somewhat stronger absorbance. Within this wavelength range, the optical absorbance of ICG is relatively low; thus, the overall absorbance is mainly dominated by the Au coating. While absorption of the microrobots solely coated with Au and Ni (yellow) was maximized somewhere in the 730- to 870-nm range, the Lipo-ICG–coated microrobots (green) showed a distinct absorption peak at the 780-nm wavelength, which is characteristic of ICG (*44*). More comprehensive analyses of the optical properties and conjugation efficiency are provided in Materials and Methods and fig. S1. Note that hemoglobin also has its isosbestic absorption point at 800-nm wavelength, which is often used to determine its concentration regardless of oxygen saturation (*45*). In addition, scattering and melanin absorption decrease at longer wavelengths (*46*). Hence, we opted for using 800-nm excitation wavelength for all subsequent experiments.

We used a volumetric OAT scanner with a spatial resolution of 150 μm (*47*) to determine the smallest detectable size of the microrobots in the presence and absence of blood. For this purpose, phantoms consisting of single microrobots embedded into agarose (Agarose-1000) and attached onto a glass slide were placed on top of a matrix array transducer that recorded the emitted signals (Fig. 2B). A droplet of blood was further added next to the microrobots to determine their relative contrast. The phantom was uniformly illuminated by a wide excitation light beam to achieve accurate comparative results. Detailed descriptions of the phantom preparation single-particle imaging with OAT are provided in Materials and Methods. Exemplary OAT and wide-field microscopy images of the microrobots coated with Lipo-ICG, Ni, and Au are shown in Fig. 2C. In particular, the OAT detection sensitivity was sufficient to detect single microrobots down to 5 μm in diameter. The discrepancy between the OAT-reconstructed particle size and their corresponding size in the microscopy images is ascribed to the 150-μm effective spatial resolution of the OAT scanner optimized for imaging at the whole-brain scale (*48*).

To accurately determine the actual contrast-to-noise ratio (CNR) of the OAT images of the microrobots, a singular value decomposition (SVD) filter was applied to a sequence of images using a customized MATLAB code. Note that the peak-to-peak magnitude of white noise amounts to approximately 3.5 times its SD. Hence, heuristically, the CNR should remain above five to clearly discern microrobots from the background. Note also that the CNR calculation in bloodless samples is basically identical to the SNR as the contrast chiefly stems from the signal generated by microrobots. To this end, SVD filtering has proven efficient in modeling and removing noise originating from different sources (*49*). Here, it was used to remove the slow varying (DC) component of the recorded signals, mainly contributed by the laser energy fluctuations (*49*), which is assumed to be additive to the actual signals from the microrobots. The presence of blood significantly increases the noise floor of the measurements (Fig. 2D), arguably due to the stronger contribution from the image reconstruction–related artefacts and other nonstationary

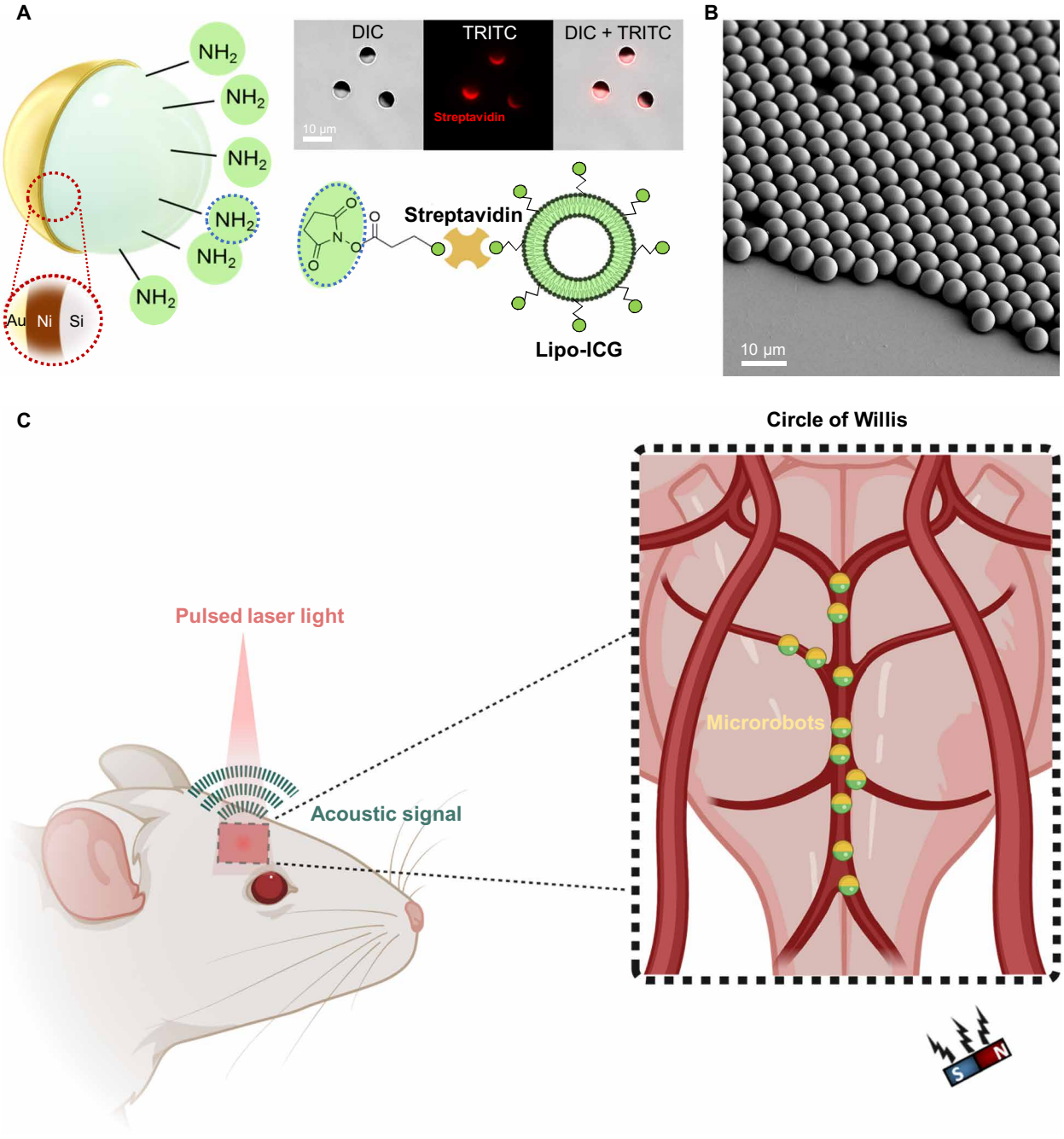

Fig. 1. Microrobot design and experimental procedure of optoacoustic tracking and magnetic manipulation. (**A**) Schematics depicting the coating composition of the microcapillary-sized magnetic microrobots used in this study. The microrobots were coated with 120-nm layer of Ni, 50-nm layer of Au, and liposomal ICG (Lipo-ICG). The Ni coating allowed for magnetic manipulation of the microrobots. Both the Au and Liposome ICG coatings were used for enhancing the OAT contrast. (Top right) A bright-field differential interference contrast (DIC) microscope image of the 5-μm-diameter Janus microrobots. The streptavidin coating necessary to bind Lipo-ICG to the microrobots is indicated by the red color coding present in the tetramethyl rhodamine isothiocyanate (TRITC) filter microscope image. (**B**) Scanning electron microscope image showing a monolayer of spherical Janus microrobots. All microrobots were coated homogenously verifying the high reproducibility of the fabrication process. (**C**) Schematic representation of the noninvasive OAT of magnetic microrobots inside the murine brain vasculature. Acoustic waves were emitted in response to the NIR light illumination with a pulsed-laser light via the photophonic effect. This enabled sensitive and high-resolution tracking of individual micrometer-sized robots inside the brain vasculature. After intravascular injection, the microrobots were transported into the circle of Willis, a prominent vascular structure inside the brain, via the natural blood circulation. A permanent magnet was used for magnetic manipulation.

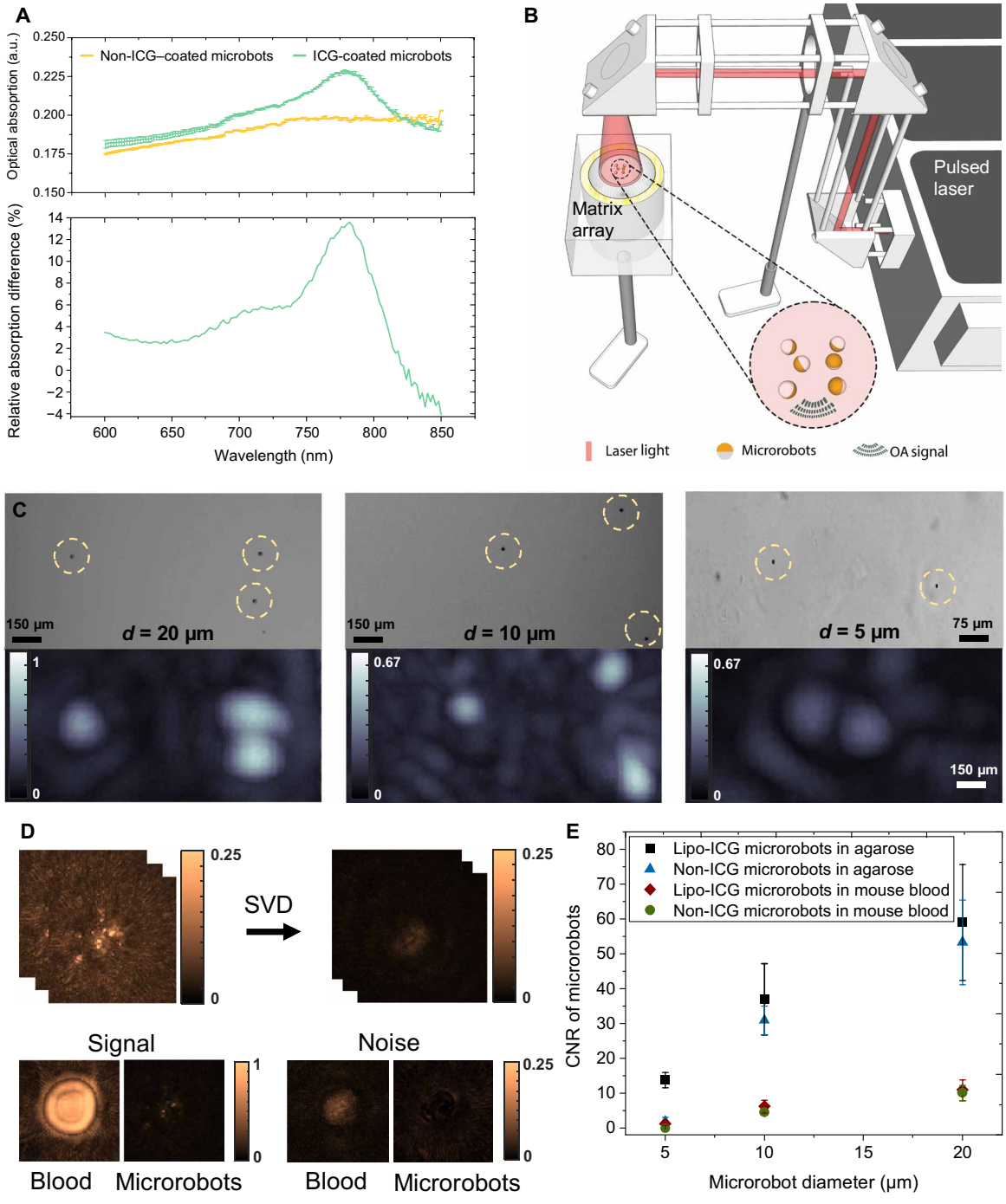

Fig. 2. Characterization of the magnetic microrobots with enhanced contrast for OAT. (**A**) Optical absorbance spectra of the 10-μm-diameter microrobots coated with 50-nm layer of Au and 120-nm layer of Ni versus the microrobots additionally coated with Lipo-ICG. The latter generally exhibited higher optical absorption in the 600- to 820-nm wavelength range while further having a distinct peak at 780 nm, corresponding to the peak extinction of ICG. The bottom graph shows the excess of optical absorption contributed by Lipo-ICG coating in relation to pure Au/Ni coating. a.u., arbitray units. (**B**) Schematic drawing of the OAT imaging setup to perform single particle imaging. A phantom consisting of individual immobilized microrobots was uniformly illuminated from above with the generated optoacoustic signals captured by a spherical matrix array transducer. (**C**) Representative OAT and wide-field microscopy images of 20-, 10-, and 5-μm microrobots. The OAT image intensity is proportional to the size of the robots. However, because of the effective 150-μm resolution of the OAT imaging system, they appear much larger in the OAT reconstructions as compared to microscopic images. The scale bars refer to both the microscopy and OAT images. (**D**) For contrast-to-noise ratio (CNR) characterization with and without the presence of blood, a singular value decomposition (SVD) filter was applied to the raw data to render the background noise levels. It is shown that bloodless samples exhibit much lower background noise. (**E**) The estimated CNR in the 600- to 870-nm range for the two types of microrobots in the presence/absence of blood. Overall, the Lipo-ICG–coated microrobots exhibit slightly higher CNR than their counterparts only coated with Ni and Au. The CNR remains proportional to the microrobot size. Furthermore, the CNR is strongly diminished in the presence of blood.

noise sources (*49*). The estimated CNR generated by the different microrobot configurations (Fig. 2E) reveals that the detected signal intensity diminishes in the presence of blood for both types of absorbing coatings. As expected, the OAT signals are also proportional to the particle diameter, although the microrobots additionally coated with Lipo-ICG had slightly higher CNR compared with their counterparts solely coated with Au and Ni. Despite the small signal difference between Lipo-ICG and non-ICG–coated microrobots, we opted for using the former in our experiments owing to the liposomes' ability to serve as carriers for cargos such as drugs or DNA (*50*). All in all, the measured CNR values indicate that all the 10-μm-diameter or larger microrobots could readily be distinguished in the presence of highly absorbing blood background.

Imaging and magnetic guidance of the microrobots in tissue phantoms

To investigate the basic feasibility of controlling and visualizing the Janus microrobots, we used an ex vivo tissue phantom, here referred as porcine intravascular guide (PIG), which included vascular network to support circulation. Specifically, branched microvessels of a porcine heart were extracted and placed onto the OAT imaging system (Fig. 3A). To mimic physiologically alternating blood flow, a perfusion pump was connected to the vessel to continuously flush it with fresh porcine blood. During the blood perfusion, the microrobots were injected into the tubing attached to the PIG phantom. The manipulation and OAT tracking of 5-, 10-, and 20-μm-sized microrobots flowing within the porcine vessel is showcased in movie S1. The maximum flow rate of 30 ml/min provided by the peristaltic pump was used to verify that the 10 frames per second (fps) volumetric imaging rate of the OAT system is adequate for real-time microrobot tracking. It can be seen that all sizes of microrobots were clearly visible even without additional postprocessing. To demonstrate controllability, the microrobots were magnetically manipulated with a neodymium (NdFeB) permanent bar magnet (40 mm by 10 mm by 10 mm) that was manually moved around the vessel to direct their motion.

As described previously, the contrast generated by the microrobots can be enhanced by applying SVD filtering in postprocessing to a series of OAT images, as showcased in Fig. 3C for 5-μm-diameter microrobots. The filtering procedure removes slowly varying background signal variations and high-frequency noise originating from blood. The isolated microrobot signals were then overlaid in green color onto a static image of the blood-filled PIG, further increasing the visibility of the microrobots (movie S2) in comparison to the unprocessed image series (movie S1). Therefore, SVD filtering plays an important role in robust tracking of microrobots having size far below the spatial resolution of the imaging system, especially in the presence of a highly absorbing blood background. For detailed information on the used SVD filtering, we refer the reader to Materials and Methods. The 20-μm-size Lipo-ICG microrobots exhibited a CNR of 10.9 in the presence of blood (Fig. 2E). Note, however, that the 150-μm spatial resolution of the OAT system greatly exceeds the single microrobot size; thus, it cannot be unequivocally determined whether the individually detected spots always correspond to single circulating microrobots.

Motion of the microrobots with and without presence of a magnetic field as well as their controlled guidance are depicted in Fig. 3D and movie S2. For the experiments, the blood flow rate was set at 1 ml/min. It can be seen that the microrobots could pass the entire vessel length within 1.3 s when passively following the flow. As soon as a bar magnet is added, the magnetic force starts pulling the microrobots against the flow direction, hence slowing them down. As a result, within the same time interval of 1.3 s, the microrobots not affected by magnetic force could move at fast 7.62 ± 4.34 mm/s velocity through the vessel, close to the actual blood flow velocity. In contrast, the microrobots experiencing a force caused by the bar magnet moved at a much slower velocity of 0.97 ± 0.27 mm/s, as indicated by the blue and yellow lines in Fig. 3D. While it would not be possible to use the same system for moving the microrobots against the physiological blood flow in major murine arteries, the applied magnetic force is strong enough to direct and decelerate the microrobots and might even be sufficient to overcome less significant flows in periphery vessels (movie S2).

We subsequently performed magnetic guidance of the microrobots clusters into a side vessel under OAT navigation (Fig. 3E). For this sequence, the microrobot passage was first occluded because of a small blood clot partially blocking part of the vessel located outside the field of view (FOV). The microrobots were released by inducing pressure with the peristaltic pump, which resulted in big clusters moving through the vessel (movie S2). These clusters were then magnetically guided into a side vessel branch. Together, these results prove the basic ability of our experimental system to control and track microrobots within blood-filled vessels in real time. Note that, because porcine vessels have a larger diameter as compared to small mammals, they also contain more blood, thus resulting in more challenging experimental conditions due to stronger background signals.

OAT imaging of the circulating microrobots in murine cerebral vasculatures

Subsequently, we explored the suitability of OAT imaging for intravascular 3D real-time tracking of microrobots circulating in an intact mouse brain vasculature (*51*). An in situ model with (Fig. 4A) and without blood background (fig. S2) was selected for this purpose to fully simulate the in vivo imaging conditions of biological tissues while having a full control of the perfusion process and avoiding potential in vivo toxicity issues of the microrobots (detailed description provided in Materials and Methods). Briefly, the sternum and rib cage of the mouse were removed after a lethal dose of ketamine. Following cessation of heart contraction, microrobots were injected into the right ventricle of the heart while simultaneously perfusing the animal with artificial cerebrospinal fluid (ACSF) or normal blood at physiological pressure levels, thus supporting nutrition and normal heart function. Owing to their small size, the microrobots could be passively transported by blood flow toward their target brain location. The beating heart provided sufficient flow to transport the microrobots through the vasculature toward the head and into the circle of Willis, a major cerebrovascular structure consisting of the basilar artery (BA), the anterior inferior cerebral artery (AICA), and the superior cerebral artery (SCA), arterioles, and capillaries.

To evaluate the influence of blood on the detection threshold and OAT image quality, the mouse was first perfused with ACSF while recording OAT images of microrobots circulating through the brain. In this way, the blood background signal was diminished, therefore increasing the detected CNR of the microrobots. It was also possible to simultaneously manipulate and track the microrobots inside the cerebral vasculature (fig. S2 and movie S3). When

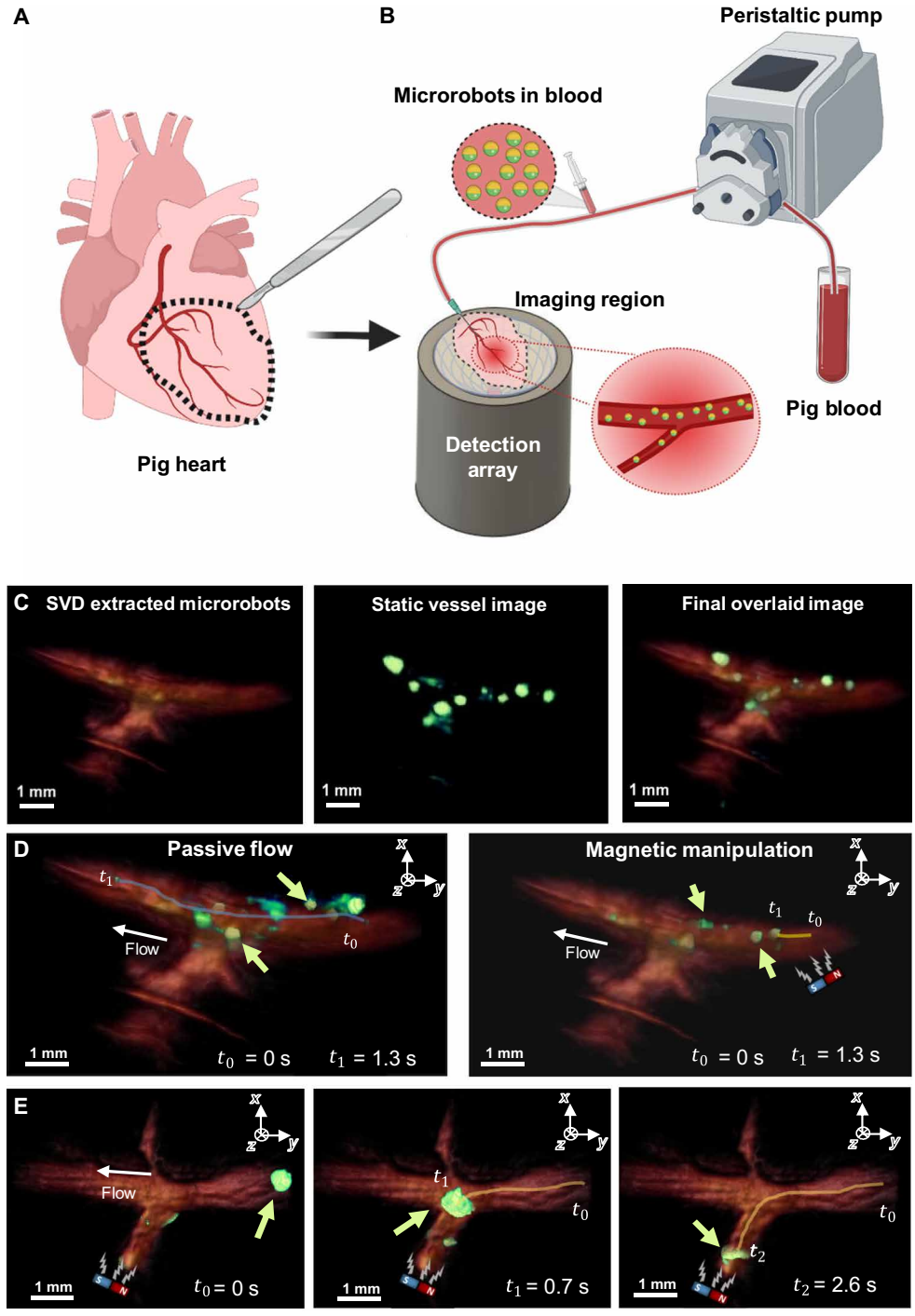

Fig. 3. OAT-based tracking and magnetic manipulation of the microrobots inside PIG phantoms. (**A**) Extraction of the coronary vessels from a pig heart. The extracted coronary vessels are used as phantoms for OAT imaging of microrobots. (**B**) Sketch of the experimental setup. Porcine blood was pumped into the phantom using a peristaltic pump. The microrobots were added into the tubing shortly before blood entered the phantom through a needle inserted into its main vessel. Once in the phantom, the microrobots were visualized with OAT and additionally manipulated by a permanent magnet. (**C**) To increase the visibility of the microrobots inside the blood-filled phantom, they were separated from the blood background using an SVD-based algorithm and overlaid in a green color over red-colored blood background. (**D**) Motion trajectory of 20-μm-diameter microrobots (green arrow) with and without the presence of the magnetic field presence. The microrobots are presented in green color, while the porcine vessel is presented in reddish color. The microrobots experiencing no magnetic force traveled along the entire vessel length within a time interval of 1.3 s (blue curve). Microrobots experiencing the magnetic force were slowed down and traveled a much shorter distance (yellow curve). (**E**) Magnetic guidance of a cluster formed by 5-μm-diameter microrobots inside the PIG phantom. After their sudden release from a narrow passage outside the field of view (FOV), the microrobots (green arrow) formed a large cluster moving through the vessel. This cluster was then guided into a side vessel branch by applying force with a permanent magnet. The magnet's position is indicated by a sketch within each image.

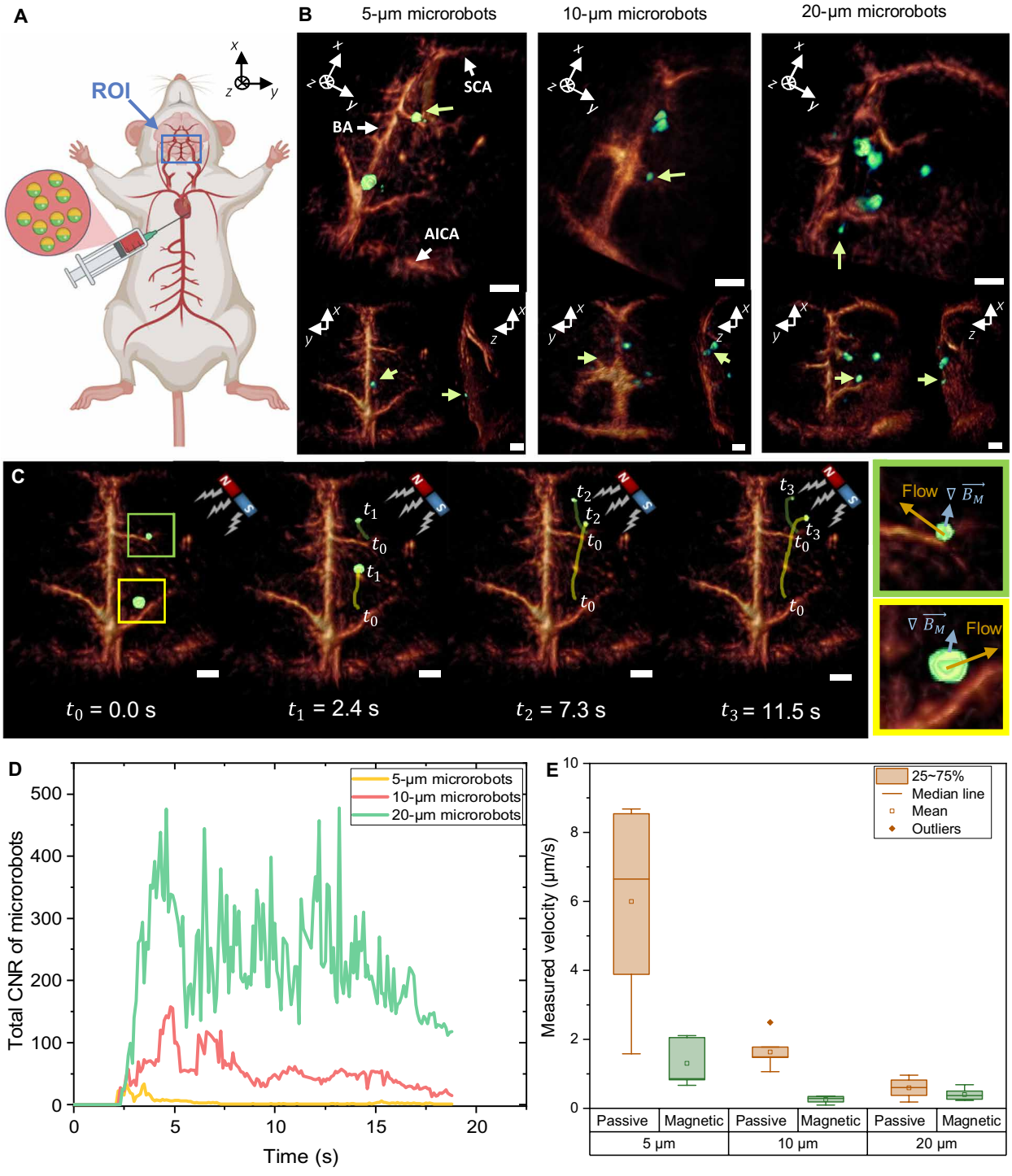

Fig. 4. Noninvasive OAT imaging of the microrobots circulating in the mouse brain vasculature. (**A**) Schematic description of the microrobot injection procedure into right atrium of the heart. The microrobots are transported with the natural blood circulation into the mouse brain where they are continuously monitored inside the FOV using the volumetric OAT. (**B**) The obtained OAT images of the Lipo-ICG–coated microrobots (green arrow) inside the circle of Willis. The circle of Willis is a prominent vascular structure consisting of the BA, the AICA, the SCA, arterioles, and capillaries. Tilted (top) and coronal and saggital projections (bottom) of the 3D images are shown. Scale bars, 1 mm. All represented images were obtained in the presence of blood circulation. (**C**) A magnet was then used to manipulate the 5-μm-diameter microrobots inside the blood-filled brain. For the regions marked in blue and green, the velocity under magnetic manipulation was estimated and compared to the passive flow of the particles. The arrows indicate the passive flow direction (yellow) and the direction in which the microrobots were attracted by the magnetic force (blue). Scale bars, 1 mm. (**D**) To validate the overall kinetics inside the FOV, a cumulative CNR of the different microrobots was calculated for each consecutive image frame, providing a measure of the amount of robots present in each frame. (**E**) The boxplot shows the measured velocity during magnetic guidance versus passive blood transport. The error bars correspond to the SEM with 5 to 14 individual microrobots measured for each parameter.

switching to the normal blood perfusion, the vascular contrast of the OAT images has readily increased (Fig. 4B). While some major vasculature in the 50- to 150-μm range—such as BA, SCA, and AICA—became clearly visible, the smaller peripheral arterioles and capillaries could not be resolved, arguably due to the relatively coarse spatial resolution of the system. Nevertheless, the 5-, 10-, and 20-μm-diameter microrobots could be clearly detected and tracked inside the circle of Willis owing to the strong contrast enhancement of the Lipo-ICG and Au-Ni nanofilm coatings. The tracking procedure can be best visualized in movie S4.

We also manipulated the 5-μm-diameter microrobots inside the mouse brain using a NdFeB permanent magnet while precisely tracking their location in real time by noninvasive OAT imaging (Fig. 4B and movie S5). Two clusters in the right periphery are seen moving in the direction of the magnet with the propulsion induced by magnetic pulling. Because of their small size, these microrobots could easily enter peripheral microvessels to find their way toward the magnet. When tracking the motion trajectory of the microrobots externally triggered by the magnetic field, it can be seen that their motion direction is almost perpendicular to that of the natural blood flow (Fig. 4B), which is not the case when no magnetic field is applied (movie S4).

To assess the overall kinetics of the microrobots in the brain, we calculated their cumulative CNR in each OAT image frame over the first 18 s following the injection (Fig. 4C). The cumulative CNR basically measures the number of microrobots present in the region of interest, being also proportional to their size, which is consistent with the in vitro results presented in Fig. 2E. All microrobots reached the circle of Willis approximately 2.4 s after being injected into the right ventricle. The CNR plot for the 5-μm microrobots shows the first peak after 2.6 s and then declining and reaching a local minimum after 3 s. The second maximum appears after 3.5 s, followed by a steady signal decline corresponding to slow clearance of microrobots from the brain. Note that some of the robots remain inside the vasculature for a longer duration with the normal blood flow unable to remove them. Similarly, the two consecutive peaks also appear in the CNR curve for the 10-μm microrobots, although at later time points. The delay can be attributed to variations in the injection speed and heart rates across different experiments. It can also be seen that the 10-μm microrobots get partially cleared over time but at a lower rate as compared to the 5-μm microrobots. In contrast, the CNR time-lapse curve for the 20 μm exhibits multiple local maxima and minima with the overall signal remaining relatively high also after prolonged durations. Most of the 20-μm-sized robots will stay inside the main arteries, such as the BA, as they are hardly able to enter peripheral arterioles. Consequently, the microrobots are transported through major brain vessels, rapidly leaving the FOV, thus resulting in abrupt CNR variations. Only few microrobots are pushed into some larger arterioles where they get arrested, which then adds up to the stronger background signal component.

Last, we compared the microrobot velocity under normal blood flow conditions versus magnetic guidance. The average speed was calculated by manually tracking the individual microrobots in the sequence of the volumetric OAT images (Fig. 4B). Figure 4D shows the measured velocity of microrobots when passively transported with the blood flow and when magnetically manipulated. The microrobots were significantly slowed down by actuation with the passive magnet (Fig. 4D), whose relatively weak strength and nondirectional nature was, however, insufficient for reversing direction of motion. As expected, the average velocity for both passive transport and magnetic manipulation decreased with increasing size of the microrobots. While the 5-μm microrobots are able to travel freely, the larger microrobots are hindered or arrested inside small capillaries. For the 20-μm microrobots, the applied magnetic force is also too weak to effectively counteract the hindered motion. All in all, our results indicate that the force induced by a permanent magnet is sufficient for moving the microrobots inside an intact murine brain vasculature while monitoring their position in real time with OAT.

DISCUSSION

The circulatory system connects all organs and tissues and hence can serve as an ideal route for microrobots to reach most target disease within the body. The small size of the human microvasculature down to 8 μm combined with high blood velocities reaching 1 mm/s makes it challenging to visualize cell-sized microrobots by means of noninvasive imaging (*21*). Our results indicate that OAT imaging serves as an emerging modality for tracking microrobots as it combines high spatiotemporal resolution in 3D with an adequate penetration depth and high specificity. OAT is also ideally suited for fully noninvasive imaging of murine brain (*47*) owing to relatively minor interference introduced to light and US propagation in the relevant wavelength and frequency ranges by a relatively thin mouse skull (fig. S4) (*52*, *53*).

In this study, we combined a high-performance volumetric OAT system with 5- to 20-μm-diameter microrobots suitable for mass production. The NIR absorption signature of the cell-sized magnetic microrobots was enhanced via gold conjugation, thus facilitating the real-time detection of individual circulating microrobots. The high spatiotemporal resolution of the imaging system allowed for 3D real-time tracking of microrobots under ex vivo–, in situ–, and in vivo–like conditions. The blood velocity inside murine brain vasculature reaches 0.15 to 8.6 mm/s (*54*–*56*), which is well within the range of the 7 mm/s mean velocity values obtained in our experiments for the 5-μm particles circulating inside murine cerebral vasculature. Imaging of circulating microrobots in the presence of highly absorbing blood background constitutes a significant leap forward toward in vivo translation of microrobotics. While large-sized robots or large particle agglomerates were previously imaged in bloodless tissues with optical absorption background in the 0.001 mm^{-1} range (*57*), whole blood has 500 times higher absorption coefficient of around 0.5 mm^{-1} at the 780-nm wavelength of interest (*58*). This makes detection of micrometer-scale objects much more challenging, especially when it comes to real-time imaging in 3D as has been reported in our work.

Because of their small size, these microrobots are able to travel even through the narrowest mouse brain microcapillaries, which enables their whole-body applicability. The microrobots could potentially be used to efficiently deliver drugs into tumors (*24*). The liposomes attached to our microrobots could additionally be used for delivering a wide range of cargos—such as drugs, cells, or DNA—while enabling the use of a broad selection of advanced contrast agents (*50*). Monocytes have a size of up to 18 μm, making them the biggest cell type passing the vascular system (*59*, *60*). Thus, in principle, given the small 5-μm size of the microrobots detectable with OAT, our method may enable single-cell tracking applications. In addition, coating the microrobots with different photochromic

proteins may allow for highly specific multiplexed OAT mapping of various cells by means of signal unmixing in the spectroscopic or temporal domains (*61*).

To allow these applications, besides tracking, precise control of the microrobots is essential for their broad applicability. As a first proof of concept, we used a permanent magnet to control the microrobots under real-time OAT guidance. Integration of a Helmholtz coil setup to generate directed magnetic fields would enable a precise 3D control of magnetic microrobots. The motion against physiological blood flow presents as another important feature of medical microrobots. Previously, surface microrollers have been shown to propel at high speeds of up to 600 μm/s, and even against the physiological blood flow, in the presence of a weak (10 mT) rotating magnetic field (200-Hz rotational frequency) (*24*). Furthermore, optimization of the actuation mechanism for specific target environments can be realized by applying a rotating magnetic field or geometric modifications (*23*), which would enable movement against the blood flow. Hence, integrating a customized electromagnetic coil setup into the OAT system is an important pillar of our future work. Depending on the target region and desired application, alternative actuation mechanisms could be used, such as acoustic (*62*, *63*) and biohybrid approaches (*64*, *65*). Besides effective propulsion and precise control, biocompatibility of the microrobots represents another important translation aspect of this technology. Encapsulating the microrobots inside the patient's own cells (*66*) and the use of biocompatible materials (*67*, *68*) would decrease biotoxicity, thus enabling long-term in vivo studies toward medical applications. In addition, the corona effect should be considered as dynamic process that can trigger a host response, leading to encapsulation of the implanted material (*69*). This response can be avoided by the use of appropriate coatings such as zwitterionic materials (*70*). Last, biodegradability is an important aspect for safe removal of microrobots from the blood stream after their tasks have been accomplished (*71*).

In conclusion, the high spatial resolution and contrast offered by OAT imaging make it a powerful modality for noninvasive tracking of microrobots. Their treatment efficiency could additionally be monitored by using molecular imaging capabilities of multispectral OAT (*72*–*74*). Our results thus pave the way toward in vivo translation of medical microrobots in intravascular environments.

MATERIALS AND METHODS

Preparation of ICG-entrapped nanoliposomes (Lipo-ICGs)

The well-established thin-film hydration technique was used for the preparation of ICG-entrapped nanoliposomes using 1,2-distearoyl-*sn*-glycero-3-phosphocholine (18:0 PC, DSPC):cholesterol:1,2-distearoyl-*sn*-glycero-3-phosphoethanolamine-*N*-[methoxy(polyethylene glycol)–2000] (18:0 PEG2000 PE):1,2-distearoyl-sn-glycero-3-phosphoethanolamine-*N*-[biotinyl PEG2000] [DSPE-PEG2000 Biotin] at 57:38:4:1 molar ratio. All phospholipids and cholesterol were purchased from Avanti Polar Lipids (Alabaster, Alabama, USA). ICG (TCI Deutschland GmbH) in methanol was added to lipid mixture in chloroform at 1:100 ICG:phospholipid molar ratio. To produce a thin lipid film, the solvent was removed with nitrogen stream and left in a vacuum desiccator overnight to remove any solvent traces. Dried lipid film was then hydrated at 20 mM lipid concentration in phosphate-buffered saline (PBS) buffer (1×, pH 7.4) for 2 hours at 55°C, with shaking at 300 rpm. Next, the multilamellar liposomal suspension was extruded for a total of 30 times using a mini-extruder (Alabaster, Alabama, USA) through polycarbonate membranes with pore sizes ranging from 1.0 to 0.4 μm to produce unilamellar liposomes. Afterward, unentrapped ICG was removed from liposomal solution via PD-10 desalting columns packed with Sephadex G-25 resin. Size and zeta potential of extruded and washed liposomes were measured with dynamic light scattering (Möbius, Wyatt Technologies). Ultraviolet-visible (UV-vis) spectra of liposomes were measured before and after the washing step and entrapment efficiency (%EE) of ICG within liposomes was calculated via $(\%EE) = \frac{\lambda_{780\,nm}\ \text{of loaded ICG}}{\lambda_{780\,nm}\ \text{of ICG fed}} \times 100$.

Preparation of ICG-liposome–coated Janus microparticles

Spherical magnetic Janus particles (5, 10, and 20 μm in diameter) were fabricated using a sputtering system. Briefly, predried monolayer of, SiO_2, silica particles (microParticles GmbH) was sequentially sputtered by 120-nm Ni and 50-nm Au using a benchtop sputter coating system (Leica EM ACE600, Leica Microsystems). Biotinylated ICG-liposomes were conjugated to the Janus particles (5, 10, and 20 μm) by using biotin-streptavidin-biotin interaction. First, amino groups were grafted to the silica side of the Janus particles to render a functional surface facilitating conjugation. To do this, 5% (v/v) (3-aminopropyl) triethoxysilane solution in ethanol was vortexed with 1×10^6 particles (in 1 ml) overnight and then incubated at 65°C for 3 hours. Subsequently, the particles were extensively washed with ethanol and then dimethyl sulfoxide (DMSO). Amino groups on the silica side were reacted with *N*-hydroxysuccinimide–conjugated biotin (EZ-Link NHS-Biotin, Thermo Fisher Scientific, Waltham, MA; 5 mg/ml in DMSO) for 2 hours to obtain biotinylated silica surface. Again, microrobots were extensively washed with DMSO and PBS (1×). To render streptavidin-end surface, the particles were treated with fluorescently labeled streptavidin (Alexa Fluor 594 conjugate, 100 μg/ml in 1× PBS, Thermo Fisher Scientific, Waltham, MA) for 1 hour, followed by a washing step by 1× PBS. As a last step, the particles were treated with biotinylated ICG-liposomes (in 1× PBS) for 1 hour.

Agarose phantoms

For imaging, a relatively low concentration of robots was embedded in an agarose phantom to ensure that the individual particles are separated by a distance larger than the effective spatial resolution of the OAT system. For this purpose, a 0.8% (w/v) agarose solution was prepared consisting of deionized (DI) water and agarose powder (Agarose-1000, Thermo Fisher Scientific, MA, USA). The solution was heated for 5 min inside a microwave to properly dissolve the agarose powder. Subsequently, it was cooled down to approximately 40°C with highly diluted microrobots immersed in PBS solution added to it. A 10-μl volume of the resulting solution was pipetted and placed onto a circular 10-mm-radius microscope glass slide. Bright-field microscopy images were taken to measure the distance between the robots and ensure that these were sufficiently separated. The phantom was eventually transported to the OAT system for image acquisition. Note that the thin glass slice barely affects US propagation in the frequency range relevant for the detection bandwidth of the spherical array used. This procedure was repeated for all microrobot types.

PIG for ex vivo particle imaging

The PIG phantom consisted of a piece of tissue extracted from a porcine heart featuring accessible blood vessels, which was obtained

from a local slaughterhouse. Its primary purpose was to test the visibility and controllability of microrobots in the presence of blood, i.e., closely mimicking the in vivo conditions. After extraction of the pericardium, we identified coronary vessels forming side branches, which are needed to test magnetic manipulation of the microrobots. A piece of tissue containing the main and side vessels was then cut out using a scalpel. This enabled blood to steadily flow out of these vessels. A needle was placed into the main vessel branch, and blood was pumped through the phantom. In this way, we were able to remove any clots or emboli that may obstruct blood flow and microrobot motion and identified leaking regions, which were sealed with tissue glue. The phantom was then placed on an agar platform filling the spherical volume enclosed by the detection array (pointing upward), and a tubing was attached to the needle. Porcine blood was perfused through this tubing using a peristaltic pump that simulated the pulsatile in vivo flow conditions and controlled the flow rate. The blood flow velocity of 7.62 ± 4.34 mm/s at a flow rate of 1 ml/min was determined by estimating the speed of passively traveling particles from a sequence of OAT images using ImageJ. Blood was collected in a custom-made blood retainer to ensure that it does not accumulate within the imaged region, which may generate strong artefacts in the images.

OAT setup

OAT imaging was performed with a Q-switched Nd:YAG-pumped optical parametric oscillator laser (SpitLight, Innolas Laser GmBH, Krailing, Germany) delivering <10-ns pulses at 10-Hz repetition rate. The laser is tuneable over a broad wavelength range spanning 680 to 1250 nm. A custom-made array consisting of 512 individual sensing elements arranged on a hemispherical surface was used to collect the optoacoustically generated signals. The spherical surface of the array has 40-mm radius and provides an angular coverage of 140° (1.31π solid angle) (*48*). Its individual elements have circular shape with a diameter of 2.5 mm and a central frequency of 5 MHz with a detection bandwidth of more than 80%. The array provides an almost isotropic spatial resolution of 150 μm (*47*). The recorded signals were simultaneously digitized by a custom-made multichannel parallel data acquisition unit (DAQ, Falkenstein Mikrosysteme GmBH, Taufkirchen, Germany) at 40 megasamples/s. The data were subsequently transferred to a PC using a 1-Gbps Ethernet connection for real-time reconstruction, data storage, and further processing. The acquisition routines were executed in MATLAB (R2020b, MathWorks Inc., USA) using a customized code. Together, this setup allowed for a real-time 3D image preview with a frame rate of 10 fps.

Agarose phantom imaging

OAT imaging of the agarose phantoms containing the microrobots was performed by guiding the laser beam with mirrors and shaping it with telescopic lenses to facilitate a more uniform illumination of the imaged volume. The diameter of the illumination beam measured 1 cm, i.e., covering a FOV of ~1 cm by 1 cm. The volume enclosed by the spherical array (pointing upward) was filled with 1% (v/v) intralipid dissolved in 1.3% (w/v) agar (bottom part) and with 1.3% (w/v) agar (top part). This provided a solid platform for placing the phantoms, ensured acoustic coupling, and protected the array's surface from being directly exposed to the intense nanosecond laser pulses. The phantoms were placed in the center of the agar platform for imaging and adjusted under the volumetric OAT preview. Data acquisition was performed with the microrobots of interest placed approximately at the center of the FOV.

In situ model of the mouse brain vasculature

To fully simulate the in vivo imaging conditions of biological tissues while avoiding potential in vivo toxicity issues of the microrobots, we used an in situ model adapted from Degtyaruk *et al.* (*51*). A total of 15 Hsd:Athymic Nude-Foxn1nu mice (Envigo, Germany) ranging in age from 8 to 12 weeks old were used for these experiments, in full compliance with the institutional guidelines and under approval from the cantonal veterinary office of Zurich. For perfusion with the ACSF (*75*), the latter was first prepared by continuously supplying it with carbogen (Linde Group, Munich, Germany). The liquid remained in a water bath (Thermo Fisher Scientific, Waltham, MA, USA) to ensure it has a physiological temperature of 37°C at the output before initiating the perfusion. Using a perfusion pump (Cole-Parmer, Vernon Hills, IL, USA) with a flow rate of 5 ml/min, the ASCF was pumped through a bubble trap connected to a glass heating coil (Radnoti LTD, Dublin, Ireland). ACSF flow continued through a physiological pressure transducer (AD Instruments, Sydney, Australia) connected to a pressure transducer simulator/tester (Utah Medical Products, Midvale, UT, USA) and a 25-gauge butterfly infusion set. This procedure was performed for at least 2 min to ensure all bubbles were removed from the liquid. The mice were intraperitoneally injected with a lethal dose of a mixture of ketamine (87.5 mg/kg; Bremer Pharma, Wabing, Germany) and xylazine (12.5 mg/kg; Bela-pharm, Vechta, Germany). In addition, 75 U of heparin (Ratiofarm GbmH, Ulm, Germany) diluted in 100 μl of 0.9% NaCl solution (Braun AG, Melsungen, Germany) was intraperitoneally injected. To ensure a stable level of deep anesthesia, the toe-pitch reflex of the mouse was tested, with the procedure continuing only after its absence was established. The mouse was positioned onto a 3.8-mm-thick silicone sheet, and its extremities were fixed in place with 28-gauge needles to minimize movement during the surgery and subsequent imaging. The silicone sheet was placed atop a transducer array holder with a 4° incline to avoid contamination of the imaging window with blood. The sheet had a small opening in the center to position the mouse head and allow the laser light to illuminate it. After the final imaging position of the head was found using the imaging preview, the head was fixated in place with Leukosilk medical tape (BSN medical, Hamburg, Germany). After the heartbeat has ceased, an incision was made from mid-abdomen to the sternum, and the ventral portion of the ribcage was removed. This allowed unhindered access to the heart. A 25-gauge butterfly needle was then used to puncture the right atrium of the mouse heart to perfuse it with ACSF. The carbogen-supplied ACSF ensured continuous cell vitality. The pressure with which ACSF flowed into the vasculature was monitored to not exceed the physiological level of 100 mmHg. In the case of in vivo–like conditions, mouse blood was used for perfusion instead of ASCF. The microrobots were immersed in 100 μl of ASCF or mouse blood depending on the experimental setup. One injection consisted of approximately 30,000 to 50,000 microrobots.

OAT imaging of mice

A dedicated holder was mounted onto the spherical matrix array for imaging mice placed in a supine position. The holder provided a slight tilt of 4° that ensured efficient drainage of blood or ACSF and prevented it from accumulating within the imaged FOV. Light

delivery was performed with an optical fiber bundle (CeramOptec GmBH, Bonn, Germany) inserted in the central cavity of the spherical array and placed at a 43-mm distance from the mouse skin. A 3.8-mm-thick silicone sheet was placed on top of the animal holder to fix the mouse with needles during the imaging session. The silicone sheet had a small opening where the mouse's head was placed to allow for OAT imaging of the brain. Acoustic coupling was ensured with 1.3% (w/v) of agar (Sigma-Aldrich, USA) dissolved in DI water filling the volume enclosed by the spherical array (pointing upward). Imaging was performed by tuning the laser wavelength to 800 nm, corresponding to the isosbestic point of hemoglobin and close to the peak absorption of ICG. For this wavelength, the per-pulse laser energy density delivered to the imaged sample was around 11 mJ/cm^2, i.e., below the American National Standards Institute (ANSI) safety limit (*76*) of 20 mJ/cm^2.

Image reconstruction

The recorded OAT data were initially bandpass-filtered within a 0.1- to 7-MHz frequency range and then deconvolved with impulse response of the detection array (*77*). Image reconstruction was carried out using a graphics processing unit implementation of a back-projection reconstruction algorithm (*78*). A uniform non-attenuating acoustic medium was assumed for reconstruction, which represents a valid approximation, considering that the acoustic impedance of agar solution is very similar to that of water and soft tissues. The speed of sound was determined by maximizing the microrobot signal in the reconstructed OAT images.

SVD filtering

In the case of in situ imaging and for determining the CNR, a SVD filter programmed in MATLAB was used. The SVD filter models and removes noise originating from various sources within the signal acquisition chain, such as those induced by the laser source. We assumed this noise to be additive with the optoacoustic signal (*49*). Consequently, the total measured signal can be denoted by $S = S_M + S_N$, with S_M and S_N being the microrobots signal and the noise, respectively. The signals simultaneously recorded by all the 512 array detection elements were saved into a data matrix. To apply the SVD filter on the acquired data matrix, the external noise was modeled by a sum of singular value components (*49*). The modeled noise was then subtracted from the acquired OAT data matrix to render the denoised signals from the microrobots. It was also used to determine the CNR of the microrobots. In the case of in situ imaging in the presence of blood background, this filtering method was additionally used to extract the dynamically moving microrobots from the background signals. The extracted microrobots were then overlaid in contrasting color in Amira Software (Thermo Fisher Scientific, USA) onto a prior acquired vascular image showing the blood-filled vessels in the region of interest.

CNR assessment

The CNR of the microrobots was calculated via CNR = S_M/σ (S_B). Here S_M, S_B, and σ are the OAT signal of the microrobots, the background signal, and its SD, respectively. The OAT signal of the microrobots and the background were extracted using the previously described SVD filter programed in MATLAB. For mouse imaging, the background was either ACSF or blood, while for the single-particle imaging in agarose phantoms, only the noise (S_N) was considered. Consequently, the determined CNR for the single-particle imaging in phantoms is basically equivalent to the signal-to-noise ratio (SNR) = S_M/σ (S_N). To determine the microrobots' kinetics inside the circle of Willis, the added-up CNR was further calculated, representing an indirect measure of the number of microrobots present within the FOV. For this, the acquired CNR values for the individual microrobots were added up for each consecutive frame.

Light spectroscopy measurement of the microrobots

The Janus microrobots with 120-nm Ni, 50-nm Au, and Lipo-ICG coating were dispersed in 1 ml of PBS and scanned in UV-vis–NIR spectroscopy device (Lambda 1050, PerkinElmer Inc.). The absolute absorbance spectra were measured against the control group, which had the same concentration of microrobots having no Lipo-ICG coating.

Statistical methods

The quantitative values were presented as one SD of the mean.

SUPPLEMENTARY MATERIALS

Supplementary material for this article is available at https://science.org/doi/10.1126/sciadv.abm9132

View/request a protocol for this paper from *Bio-protocol*.

REFERENCES AND NOTES

1. M. Sitti, *Mobile Microrobotics* (MIT Press, 2017).
2. H. Ceylan, I. C. Yasa, U. Kilic, W. Hu, M. Sitti, Translational prospects of untethered medical microrobots. *Prog. Biomed. Eng.* **1**, 012002 (2019).
3. C. K. Schmidt, M. Medina-Sánchez, R. J. Edmondson, O. G. Schmidt, Engineering microrobots for targeted cancer therapies from a medical perspective. *Nat. Commun.* **11**, 5618 (2020).
4. F. Soto, R. Chrostowski, Frontiers of medical micro/nanorobotics: In vivo applications and commercialization perspectives toward clinical uses. *Front. Bioeng. Biotechnol.* **6**, 170 (2018).
5. M. Medina-Sánchez, H. Xu, O. G. Schmidt, Micro- and nano-motors: The new generation of drug carriers. *Ther. Deliv.* **9**, 303–316 (2018).
6. S. K. Srivastava, G. Clergeaud, T. L. Andresen, A. Boisen, Micromotors for drug delivery in vivo: The road ahead. *Adv. Drug Deliv. Rev.* **138**, 41–55 (2019).
7. H. Xu, M. Medina-Sánchez, V. Magdanz, L. Schwarz, F. Hebenstreit, O. G. Schmidt, Sperm-hybrid micromotor for targeted drug delivery. *ACS Nano* **12**, 327–337 (2018).
8. H. Ceylan, I. C. Yasa, O. Yasa, A. F. Tabak, J. Giltinan, M. Sitti, 3D-printed biodegradable microswimmer for theranostic cargo delivery and release. *ACS Nano* **13**, 3353–3362 (2019).
9. U. Bozuyuk, O. Yasa, I. C. Yasa, H. Ceylan, S. Kizilel, M. Sitti, Light-triggered drug release from 3D-printed magnetic chitosan microswimmers. *ACS Nano* **12**, 9617–9625 (2018).
10. B. W. Park, J. Zhuang, O. Yasa, M. Sitti, Multifunctional bacteria-driven microswimmers for targeted active drug delivery. *ACS Nano* **11**, 8910–8923 (2017).
11. H. Xu, M. Medina-Sánchez, M. F. Maitz, C. Werner, O. G. Schmidt, Sperm micromotors for cargo delivery through flowing blood. *ACS Nano* **14**, 2982–2993 (2020).
12. M. Medina-Sánchez, L. Schwarz, A. K. Meyer, F. Hebenstreit, O. G. Schmidt, Cellular cargo delivery: Toward assisted fertilization by sperm-carrying micromotors. *Nano Lett.* **16**, 555–561 (2016).
13. I. C. Yasa, A. F. Tabak, O. Yasa, H. Ceylan, M. Sitti, 3D-printed microrobotic transporters with recapitulated stem cell niche for programmable and active cell delivery. *Adv. Funct. Mater.* **29**, 1808992 (2019).
14. F. Qiu, S. Fujita, R. Mhanna, L. Zhang, B. R. Simona, B. J. Nelson, Magnetic helical microswimmers functionalized with lipoplexes for targeted gene delivery. *Adv. Funct. Mater.* **25**, 1666–1671 (2015).
15. A. Chałupniak, E. Morales-Narváez, A. Merkoçi, Micro and nanomotors in diagnostics. *Adv. Drug Deliv. Rev.* **95**, 104–116 (2015).
16. J. Leclerc, H. Zhao, D. Bao, A. T. Becker, In vitro design investigation of a rotating helical magnetic swimmer for combined 3-D navigation and blood clot removal. *IEEE Trans. Robot.* **36**, 975–982 (2020).
17. R. Cheng, W. Huang, L. Huang, B. Yang, L. Mao, K. Jin, Q. ZhuGe, Y. Zhao, Acceleration of tissue plasminogen activator-mediated thrombolysis by magnetically powered nanomotors. *ACS Nano* **8**, 7746–7754 (2014).
18. I. S. M. Khalil, A. F. Tabak, K. Sadek, D. Mahdy, N. Hamdi, M. Sitti, Rubbing against blood clots using helical robots: Modeling and in vitro experimental validation. *IEEE Robot. Autom. Lett.* **2**, 927–934 (2017).

19. Y. Alapan, O. Yasa, O. Schauer, J. Giltinan, A. F. Tabak, V. Sourjik, M. Sitti, Soft erythrocyte-based bacterial microswimmers for cargo delivery. *Sci. Robot.* **3**, eaar4423 (2018).
20. J. Park, C. Jin, S. Lee, J. Y. Kim, H. Choi, Magnetically actuated degradable microrobots for actively controlled drug release and hyperthermia therapy. *Adv. Healthc. Mater.* **8**, 1900213 (2019).
21. B. Müller, S. Lang, M. Dominietto, M. Rudin, G. Schulz, H. Deyhle, M. Germann, F. Pfeiffer, C. David, T. Weitkamp, High-resolution tomographic imaging of microvessels, in *Developments in X-Ray Tomography VI 7078*, S. R. Stock, Ed. (International Society for Optics and Photonics, 2008).
22. B. J. Nelson, I. K. Kaliakatsos, J. J. Abbott, Microrobots for minimally invasive medicine. *Annu. Rev. Biomed. Eng.* **12**, 55–85 (2010).
23. U. Bozuyuk, Y. Alapan, A. Aghakhani, M. Yunusa, M. Sitti, Shape anisotropy-governed locomotion of surface microrollers on vessel-like microtopographies against physiological flows. *Proc. Natl. Acad. Sci. U.S.A.* **118**, e2022090118 (2021).
24. Y. Alapan, U. Bozuyuk, P. Erkoc, A. C. Karacakol, M. Sitti, Multifunctional surface microrollers for targeted cargo delivery in physiological blood flow. *Sci. Robot.* **5**, eaba5726 (2020).
25. X. Yan, Q. Zhou, M. Vincent, Y. Deng, J. Yu, J. Xu, T. Xu, T. Tang, L. Bian, Y.-X. J. Wang, K. Kostarelos, L. Zhang, Multifunctional biohybrid magnetite microrobots for imaging-guided therapy. *Sci. Robot.* **2**, eaaq1155 (2017).
26. S. Jeong, H. Choi, G. Go, C. Lee, K. S. Lim, D. S. Sim, M. H. Jeong, S. Y. Ko, J. O. Park, S. Park, Penetration of an artificial arterial thromboembolism in a live animal using an intravascular therapeutic microrobot system. *Med. Eng. Phys.* **38**, 403–410 (2016).
27. S. Pane, V. Iacovacci, M. H. D. Ansari, A. Menciassi, Ultrasound-guided navigation of a magnetic microrobot using acoustic phase analysis. *Sci. Rep.* **11**, 23239 (2021).
28. F. Ullrich, C. Bergeles, J. Pokki, O. Ergeneman, S. Erni, G. Chatzipirpiridis, S. Pané, C. Framme, B. J. Nelson, Mobility experiments with microrobots for minimally invasive intraocular surgery. *Investig. Ophthalmol. Vis. Sci.* **54**, 2853–2863 (2013).
29. A. Aziz, M. Medina-Sánchez, N. Koukourakis, J. Wang, R. Kuschmierz, H. Radner, J. W. Czarske, O. G. Schmidt, Real-time IR tracking of single reflective micromotors through scattering tissues. *Adv. Funct. Mater.* **29**, 1905272 (2019).
30. D. Vilela, U. Cossío, J. Parmar, A. M. Martínez-Villacorta, V. Gómez-Vallejo, J. Llop, S. Sánchez, Medical imaging for the tracking of micromotors. *ACS Nano* **12**, 1220–1227 (2018).
31. A. Graham Bell, On the production and reproduction of sound by light. *Am. J. Sci.* **s3-20**, 305–324 (1880).
32. S. Manohar, D. Razansky, Photoacoustics: A historical review. *Adv. Opt. Photon.* **8**, 586–617 (2016).
33. X. L. Deán-Ben, S. Gottschalk, B. Mc Larney, S. Shoham, D. Razansky, Advanced optoacoustic methods for multi-scale imaging of in vivo dynamics. *Chem. Soc. Rev.* **46**, 2158–2198 (2017).
34. P.-C. Li, C. R. C. Wang, D. B. Shieh, C. W. Wei, C. K. Liao, C. Poe, S. Jhan, A. A. Ding, Y. N. Wu, In vivo photoacoustic molecular imaging with simultaneous multiple selective targeting using antibody-conjugated gold nanorods. *Opt. Express* **16**, 18605–18615 (2008).
35. V. Ntziachristos, D. Razansky, Molecular imaging by means of multispectral optoacoustic tomography (MSOT). *Chem. Rev.* **110**, 2783–2794 (2010).
36. V. Gujrati, A. Mishra, V. Ntziachristos, Molecular imaging probes for multi-spectral optoacoustic tomography. *Chem. Commun.* **53**, 4653–4672 (2017).
37. D. Razansky, N. C. Deliolanis, C. Vinegoni, V. Ntziachristos, Deep tissue optical and optoacoustic molecular imaging technologies for pre-clinical research and drug discovery. *Curr. Pharm. Biotechnol.* **13**, 504–522 (2012).
38. P. Beard, Biomedical photoacoustic imaging. *Interface Focus* **1**, 602–631 (2011).
39. Z. Wu, L. Li, Y. Yang, P. Hu, Y. Li, S.-Y. Yang, L. V. Wang, W. Gao, A microrobotic system guided by photoacoustic computed tomography for targeted navigation in intestines in vivo. *Sci. Robot.* **4**, eaax0613 (2019).
40. A. Aziz, M. Medina-Sánchez, J. Claussen, O. G. Schmidt, Real-time optoacoustic tracking of single moving micro-objects in deep phantom and ex vivo tissues. *Nano Lett.* **19**, 6612–6620 (2019).
41. U. Bozuyuk, E. Suadiye, A. Aghakhani, N. O. Dogan, J. Lazovic, M. E. Tiryaki, M. Schneider, A. C. Karacakol, S. O. Demir, G. Richter, M. Sitti, High-performance magnetic FePt (L1 0) surface microrollers towards medical imaging-guided endovascular delivery applications. *Adv. Funct. Mater.* **32**, 2109741 (2021).
42. A. Aziz, J. Holthof, S. Meyer, O. G. Schmidt, M. Medina-Sánchez, Dual ultrasound and photoacoustic tracking of magnetically driven micromotors: From in vitro to in vivo. *Adv. Healthc. Mater.* **10**, 2101077 (2021).
43. L. Xie, X. Pang, X. Yan, Q. Dai, H. Lin, J. Ye, Y. Cheng, Q. Zhao, X. Ma, X. Zhang, G. Liu, X. Chen, Photoacoustic imaging-trackable magnetic microswimmers for pathogenic bacterial infection treatment. *ACS Nano* **14**, 2880–2893 (2020).
44. A. Fernandez-Fernandez, R. Manchanda, T. Lei, D. A. Carvajal, Y. Tang, S. Z. R. Kazmi, A. J. McGoron, Comparative study of the optical and heat generation properties of IR820 and indocyanine green. *Mol. Imaging* **11**, 99–113 (2012).
45. E. W. Richter, R. Sniecinski, Data interpretation in anesthesia. *Anesth. Analg.* **127**, 297 (2018).
46. G. Zonios, A. Dimou, I. Bassukas, D. Galaris, A. Tsolakidis, E. Kaxiras, Melanin absorption spectroscopy: New method for noninvasive skin investigation and melanoma detection. *J. Biomed. Opt.* **13**, 014017 (2008).
47. S. Gottschalk, O. Degtyaruk, B. Mc Larney, J. Rebling, M. A. Hutter, X. L. Deán-Ben, S. Shoham, D. Razansky, Rapid volumetric optoacoustic imaging of neural dynamics across the mouse brain. *Nat. Biomed. Eng.* **3**, 392–401 (2019).
48. B. McLarney, J. Rebling, Z. Chen, X. L. Deán-Ben, S. Gottschalk, D. Razansky, Uniform light delivery in volumetric optoacoustic tomography. *J. Biophotonics* **12**, e201800387 (2019).
49. E. R. Hill, W. Xia, M. J. Clarkson, A. E. Desjardins, Identification and removal of laser-induced noise in photoacoustic imaging using singular value decomposition. *Biomed. Opt. Express* **8**, 68–77 (2017).
50. F. Qiu, R. Mhanna, L. Zhang, Y. Ding, S. Fujita, B. J. Nelson, Artificial bacterial flagella functionalized with temperature-sensitive liposomes for controlled release. *Sensors Actuators B Chem.* **196**, 676–681 (2014).
51. O. Degtyaruk, B. Mc Larney, X. Deán-Ben, S. Shoham, D. Razansky, Optoacoustic calcium imaging of deep brain activity in an intracardially perfused mouse brain model. *PhotoDermatology* **6**, 67 (2019).
52. H. Soleimanzad, H. Gurden, F. Pain, Optical properties of mice skull bone in the 455- to 705-nm range. *J. Biomed. Opt.* **22**, 010503 (2017).
53. M. Kneipp, J. Turner, H. Estrada, J. Rebling, S. Shoham, D. Razansky, Effects of the murine skull in optoacoustic brain microscopy. *J. Biophotonics* **9**, 117–123 (2016).
54. X. Chen, Y. Jiang, S. Choi, R. Pohmann, K. Scheffler, D. Kleinfeld, X. Yu, Assessment of single-vessel cerebral blood velocity by phase contrast fMRI. *PLoS Biol.* **19**, e3000923 (2021).
55. M. Unekawa, M. Tomita, Y. Tomita, H. Toriumi, K. Miyaki, N. Suzuki, RBC velocities in single capillaries of mouse and rat brains are the same, despite 10-fold difference in body size. *Brain Res.* **1320**, 69–73 (2010).
56. W. I. Rosenblum, Erythrocyte velocity and a velocity pulse in minute blood vessels on the surface of the mouse brain. *Circ. Res.* **24**, 887–892 (1969).
57. E. L. Wisotzky, F. C. Uecker, S. Dommerich, A. Hilsmann, P. Eisert, P. Arens, Determination of optical properties of human tissues obtained from parotidectomy in the spectral range of 250 to 800 nm. *J. Biomed. Opt.* **24**, 1–7 (2019).
58. M. Friebel, A. Roggan, G. Müller, M. Meinke, Determination of optical properties of human blood in the spectral range 250 to 1100 nm using Monte Carlo simulations with hematocrit-dependent effective scattering phase functions. *J. Biomed. Opt.* **11**, 034021 (2006).
59. Y. C. Fung, *Biomechanics* (Springer-Verlag, 1997).
60. F. J. Baker, R. E. Silverton, *Introduction* (Elsevier, 1976).
61. K. Mishra, M. Stankevych, J. P. Fuenzalida-Werner, S. Grassmann, V. Gujrati, Y. Huang, U. Klemm, V. R. Buchholz, V. Ntziachristos, A. C. Stiel, Multiplexed whole-animal imaging with reversibly switchable optoacoustic proteins. *Sci. Adv.* **6**, eaaz6293 (2020).
62. A. Aghakhani, O. Yasa, P. Wrede, M. Sitti, Acoustically powered surface-slipping mobile microrobots. *Proc. Natl. Acad. Sci.* **117**, 3469–3477 (2020).
63. L. Ren, N. Nama, J. M. McNeill, F. Soto, Z. Yan, W. Liu, W. Wang, J. Wang, T. E. Mallouk, 3D steerable, acoustically powered microswimmers for single-particle manipulation. *Sci. Adv.* **5**, eaax3084 (2019).
64. I. C. Yasa, H. Ceylan, U. Bozuyuk, A.-M. Wild, M. Sitti, Elucidating the interaction dynamics between microswimmer body and immune system for medical microrobots. *Sci. Robot.* **5**, eaaz3867 (2020).
65. M. Medina-Sánchez, V. Magdanz, L. Schwarz, H. Xu, O. G. Schmidt, Spermbots: Concept and applications, in *Proceedings of the 6th International Conference on Biomimetic and Biohybrid Systems* (Springer, 2017).
66. H. Ceylan, N. O. Dogan, I. C. Yasa, M. N. Musaoglu, Z. U. Kulali, M. Sitti, 3D printed personalized magnetic micromachines from patient blood – derived biomaterials. *Sci. Adv.* **7**, eabh0273 (2021).
67. G. Go, S.-G. Jeong, A. Yoo, J. Han, B. Kang, S. Kim, K. T. Nguyen, Z. Jin, C.-S. Kim, Y. R. Seo, J. Y. Kang, J. Y. Na, E. K. Song, Y. Jeong, J. K. Seon, J.-O. Park, E. Choi, Human adipose-derived mesenchymal stem cell-based medical microrobot system for knee cartilage regeneration in vivo. *Sci. Robot.* **5**, eaay6626 (2020).
68. S. Jeon, S. Kim, S. Ha, S. Lee, E. Kim, S. Y. Kim, S. H. Park, J. H. Jeon, S. W. Kim, C. Moon, B. J. Nelson, J.-Y. Kim, S.-W. Yu, H. Choi, Magnetically actuated microrobots as a platform for stem cell transplantation. *Sci. Robot.* **4**, eaav4317 (2019).
69. D. W. Grainger, All charged up about implanted biomaterials. *Nat. Biotechnol.* **31**, 507–509 (2013).
70. L. Zhang, Z. Cao, T. Bai, L. Carr, J. R. Ella-Menye, C. Irvin, B. D. Ratner, S. Jiang, Zwitterionic hydrogels implanted in mice resist the foreign-body reaction. *Nat. Biotechnol.* **31**, 553–556 (2013).
71. J. Llacer-Wintle, A. Rivas-Dapena, X. Z. Chen, E. Pellicer, B. J. Nelson, J. Puigmartí-Luis, S. Pané, Biodegradable small-scale swimmers for biomedical applications. *Adv. Mater.* **33**, 2102049 (2021).

72. A. Ron, S. K. Kalva, V. Periyasamy, X. L. Deán-Ben, D. Razansky, Flash scanning volumetric optoacoustic tomography for high resolution whole-body tracking of nanoagent kinetics and biodistribution. *Laser Photonics Rev.* **15**, 2000484 (2021).
73. A. Karlas, M. Kallmayer, M. Bariotakis, N. A. Fasoula, E. Liapis, F. Hyafil, J. Pelisek, M. Wildgruber, H. H. Eckstein, V. Ntziachristos, Multispectral optoacoustic tomography of lipid and hemoglobin contrast in human carotid atherosclerosis. *PhotoDermatology* **23**, 100283 (2021).
74. J. W. Baik, H. Kim, M. Son, J. Choi, K. G. Kim, J. H. Baek, Y. H. Park, J. An, H. Y. Choi, S. Y. Ryu, J. Y. Kim, K. Byun, C. Kim, Intraoperative label-free photoacoustic histopathology of clinical specimens. *Laser Photonics Rev.* **15**, 2100124 (2021).
75. O. Von Bohlen, The isolated mammalian brain: An in vivo preparation suitable for pathway tracing. *Eur. J. Neurosci.* **11**, 1096–1100 (1999).
76. American National Standard for Safety Use of Lasers, ANSI Z136. (Laser Institute of America, 2014).
77. A. Rosenthal, V. Ntziachristos, D. Razansky, Model-based optoacoustic inversion with arbitrary-shape detectors. *Med. Phys.* **38**, 4285–4295 (2011).
78. X. L. Deán-Ben, A. Ozbek, D. Razansky, Volumetric real-time tracking of peripheral human vasculature with GPU-accelerated three-dimensional optoacoustic tomography. *IEEE Trans. Med. Imaging* **32**, 2050–2055 (2013).

Acknowledgments: We would like to acknowledge H. Estrada for valuable advice with skull measurements. **Funding:** The schematics of this paper were created with BioRender.com. D.R. acknowledges support from the European Research Council (ERC) grant ERC-2015-CoG-682379 and the National Institutes of Health grant UF1-NS107680. M.S. acknowledges support from the Max Planck Society and ERC Advanced Grant SoMMoR (grant no. 834531). **Author contributions:** P.W., X.L.D.-B., M.S., and D.R. conceived the idea. P.W., O.D., S.K.K., and X.L.D.-B. performed the imaging experiments. U.B., A.A., and B.A. fabricated and characterized the microrobots. M.S. and D.R. supervised and funded the research. All authors contributed to writing and revising the manuscript. **Competing interests:** The authors declare that they have no competing interests. **Data and materials availability:** All data generated or analyzed during this study are included in the published article and its Supplementary Materials. Code availability: The code for SVD filtering is available on Zenodo with the DOI: 10.5281/zenodo.5795071.

Submitted 20 October 2021
Accepted 25 March 2022
Published 11 May 2022
10.1126/sciadv.abm9132